Article:
Gomez-Rivas, E, Griera, A, Llorens, M-G et al. (3 more authors) (2017) Subgrain Rotation Recrystallization During Shearing: Insights From Full-Field Numerical Simulations of Halite Polycrystals. Journal of Geophysical Research: Solid Earth, 122 (11). pp. 8810-8827. ISSN 2169-9313

https://doi.org/10.1002/2017JB014508

Subgrain rotation recrystallization during shearing: insights from full-field numerical simulations of halite polycrystals

E. Gomez-Rivas[1], A. Griera[2], M. -G. Llorens[3], P. D. Bons[3], R. A. Lebensohn[4], and S. Piazolo[5]

[1]School of Geosciences, King's College, University of Aberdeen, Aberdeen AB24 3UE, United Kingdom

[2]Departament de Geologia, Universitat Autònoma de Barcelona, 08193 Bellaterra (Cerdanyola del Vallès), Spain

[3]Department of Geosciences, Eberhard Karls University of Tübingen, Wilhelmstr. 56, 72074 Tübingen, Germany

[4]Materials Science and Technology Division, Los Alamos National Laboratory, Los Alamos NM 87545, USA

[5]School of Earth and Environment, University of Leeds, Leeds LS2 9JT, United Kingdom

Corresponding author: Enrique Gomez-Rivas (e.gomez-rivas@abdn.ac.uk)

Key Points:

- Full-field numerical simulations of subgrain rotation recrystallization, able to reproduce experiments, are presented for first time
- Intracrystalline recovery strongly decreases grain size reduction but does not change crystal preferred orientations
- Mean subgrain misorientations can be used as a strain gauge for polycrystals undergoing recrystallization, following a universal law

Abstract

We present, for the first time, results of full-field numerical simulations of subgrain rotation recrystallization of halite polycrystals during simple shear deformation. The series of simulations show how microstructures are controlled by the competition between (i) grain size reduction by dislocation creep and (ii) intracrystalline recovery encompassing subgrain coarsening (SGC) by coalescence through rotation and alignment of the lattices of neighboring subgrains. A strong grain size reduction develops in models without intracrystalline recovery, as a result of the formation of high-angle grain boundaries when local misorientations exceed 15°. The activation of subgrain coarsening associated with recovery decreases the stored strain energy and results in grains with low intracrystalline heterogeneities. However, this type of recrystallization does not significantly modify crystal preferred orientations. Lattice orientation and grain boundary maps reveal that this full-field modelling approach is able to successfully reproduce the evolution of dry halite microstructures from laboratory deformation experiments, thus opening new opportunities in this field of research. We demonstrate how the mean subgrain boundary misorientations can be used to estimate the strain accommodated by dislocation creep using a universal scaling exponent of about 2/3, as predicted by theoretical models. In addition, this strain gauge can be potentially applied to estimate the intensity of intracrystalline recovery, associated with temperature, using EBSD maps in areas with strain gradients.

1 Introduction

Understanding rock deformation microstructures is essential to unravel tectonic processes and to predict physical properties of crustal and mantle rocks. Polycrystalline aggregates typically develop crystal preferred orientations (CPO) and may lead to strongly anisotropic behavior when they are deformed by dislocation creep [*Urai et al.*, 1986; *Passchier and Trouw*, 2005]. Halite (NaCl) is a widely used mineral to understand the behavior of rocks deformed in the ductile regime. It has very special properties, since it is nearly incompressible, highly soluble, has a very low permeability, and can flow ductily in the solid state under relatively low stresses. Therefore, it is widely used for deformation and recrystallization experiments, and is an accepted analogue material for silicates that deform ductily at much higher temperatures and pressures [e.g., *Guillope and Poirier*, 1979]. At low temperature and dry conditions halite deforms by dislocation creep, with subgrain rotation [SGR; e.g., *Urai et al.*, 1986; *Trimby et al.*, 2000] being the dominant recrystallization mechanism [regime 2 of *Hirth and Tullis*, 1992]. This results in an anisotropic behavior with the development of strong intracrystalline heterogeneities. SGR is linked to the formation of subgrain boundaries as a consequence of strain, and is also associated with the reduction of free energy by the activation of intracrystalline processes that result in the reorganization of subgrains (recovery) [e.g., *Halfpenny et al.*, 2006; *Karato*, 2012]. Two main processes influence the formation of subgrain boundaries: (i) annihilation of dislocations of opposite signs and (ii) polygonization, which consists on the alignment of dislocations [*Humphreys and Hatherly*, 2004; *Borthwick and Piazolo*, 2010]. In such a situation, dislocations move and interact to form low-angle subgrain boundaries (LAGB), leading to an increase in misorientation between subgrains [*Urai et al.*, 1986]. Progressive strain increases this misorientation angle until a critical value is reached, allowing the subgrains to become new grains as their boundaries achieve high angles (HAGB). This critical angle ranges between 10º and 15º, when the distances between dislocations are similar to the atomic ones [*Karato*, 2012]. This process results in a strong grain size reduction with increasing deformation and the formation of recrystallized grains that tend to have a size similar to that of the subgrains.

Several studies have analyzed the development of low-angle boundaries and how misorientations are related to strain. Two types of dislocation boundaries are distinguished [*Kuhlmann-Wilsdorf and Hansen*, 1991; *Pantleon*, 2001]: incidental dislocation boundaries (IDBs), which result from statistical mutual trapping of dislocations, and geometrically necessary boundaries (GNBs), which form due to the activation of different sets of slip systems or the different activity of the same set of slip systems on each side of the boundary. *Hughes et al.* [1997; 1998; 2003] proposed a material-independent universal scaling behavior between the average misorientation (θ_{av}) of the system and the natural strain (ε) using metal deformation experiments. *Pantleon* [1997; 1998; 2001] and *Sethna and Coffman* [2003] confirmed these scaling laws and provided explanations for the misorientation distributions and their scaling laws, focusing on metals. *Pennock et al.* [2005] proposed a new approach, in which misorientations are measured on a grain basis, and obtained a slightly different scaling law. If this universal scaling also applies to rocks, this strain gauge can be a useful tool, since it allows the estimation of strain by measuring misorientations from deformed samples with electron backscatter diffraction analysis (EBSD). However, this method has only been applied to cases of coaxial deformation, and the interplay between dislocation creep and synchronous recovery of intracrystalline defects or post-deformation annealing can result in a substantial modification of the microstructure and the reduction of subgrain misorientations associated with the decrease of free energy (i.e., boundary and strain stored energies). This process can strongly affect microstructures in halite and other materials [*Borthwick and Piazolo*, 2010], thus potentially hindering the use of subgrain misorientations as a strain gauge.

Numerical simulation is a very useful tool that can complement the study of natural and experimental samples, because it allows analysis of the effects of single or coupled deformation processes in a wide range of deformation scenarios and for systems with variable material properties. Moreover, simulations can overcome some of the limitations of experiments, because variable sample sizes can be studied, and also high finite strain can be achieved at low strain rates. The numerical evolution of textures and crystallographic preferred orientations (CPOs) of polycrystalline aggregates has been widely investigated using kinematic [e.g., D-REX, *Kaminsky and Ribe*, 2001] and self-consistent approaches, such as the viscoplastic self-consistent formulation (VPSC) [*Wenk et al.*, 1989; *Lebensohn et al.*, 2003]. The VPSC method models the reorientation of grains through intracrystalline slip and grain interaction assuming a homogenous equivalent matrix. It adequately predicts lattice rotations depending on the slip system activity, and shows results similar to those observed in experiments or predicted by finite element models [see *Lebensohn et al.*, 2003]. However, these methods have the limitation that they only simulate viscoplastic deformation and that dynamic recrystallization is only incorporated by using probabilistic models. For instance, *Signorelli and Tommasi* [2015] successfully simulated subgrain rotation recrystallization and the resulting CPOs in olivine with the VPSC approach, but using an ad hoc probabilistic law for grain size reduction. In a similar way, the kinematical code D-REX [*Kaminsky and Ribe*, 2001] incorporates dynamic recrystallization processes through two dimensionless parameters that account for grain boundary migration and nucleation. However, all these methods are not full-field, and therefore cannot model the full range of intracrystalline heterogeneities and intercrystalline interactions that develop in polycrystals. Apart from these disadvantages, all the methods mentioned above do not allow to visualize the explicit evolution of the microstructures with deformation and are only restricted to the texture, and sometimes grain size evolution.

Recently, a full-field crystal viscoplastic approach based on the Fast Fourier Transform (VPFFT) [*Lebensohn*, 2001; *Lebensohn et al.*, 2008] has been integrated within the ELLE software platform [*Jessell et al.*, 2001] to simulate coupled geological processes during deformation and metamorphism [*Griera et al.*, 2011; *Griera et al.*, 2013; *Llorens et al.*, 2016a; *Llorens et al.,* 2016b; *Llorens et al.,* 2017; *Steinbach et al*., 2017]. In this model the laws controlling grain size reduction and intracrystalline recovery are defined from the mapped variation of misorientations related to the relative misfit between local lattice orientations, providing a more realistic framework for the simulation of microstructures. Additionally, this code is able to simulate the spatial evolution of deformation, which has a strong influence on the resulting microstructures, and can model processes such as strain localization up to high strain [*Llorens et al.*, 2016b]. This method allows a full control on the relative contribution of each deformation mechanism during microstructure evolution. Finally, although VPFFT/ELLE is expensive in computational time, it provides results in the same format as those obtained with EBSD analysis from natural and experimental samples, allowing direct comparisons.

This contribution presents numerical simulations of pure halite deformation and recrystallization under dry conditions at relatively low temperatures (< 200°C) up to a shear strain of four, with the aim of understanding the behavior of polycrystalline aggregates undergoing subgrain rotation recrystallization. At these temperatures, the rate of grain boundary migration (GBM) is negligible, hence only intracrystalline recovery is considered here. We briefly introduce the VPFFT/ELLE method and present a series of numerical experiments in which a polycrystalline aggregate is deformed varying the strength along halite slip systems. Viscoplastic deformation is coupled with a process that simulates intracrystalline recovery associated with the decrease of free energy by subgrain rotation. In this way, we evaluate the competition between dislocation creep and recovery, and show how the interplay between these processes influences the resulting microstructures. Moreover, we assess the use of subgrain misorientations as a strain gauge in situations of simple shear deformation incorporating dynamic recrystallization by subgrain rotation and recovery. Since most rocks undergo intracrystalline recovery during and after deformation, we aim to understand how this process affects the strain gauge and whether misorientations can also be used to unravel the environmental conditions associated with recovery (i.e., temperature). The numerical results match well those from coaxial experiments by *Pennock et al.* [2005], torsion experiments by *Armann* [2008] or CPO modelling by *Wenk et al.* [2009], and allow the study of microstructures in a much wider range of conditions than those in the laboratory. This numerical method is not restricted to halite, but can also be applied to less studied and less accessible polycrystalline aggregates of minerals with a similar structure and slip systems, such as magnesiowüstite in the lower mantle.

2 Methods

The microstructural evolution of a pure halite polycrystalline aggregate during deformation creep and recrystallization is numerically simulated using the software platform ELLE [*Jessell et al.*, 2001; http://www.elle.ws]. ELLE is open-source software for the simulation of rock microstructures during deformation and metamorphism. Our models are based on the coupling of a full-field viscoplastic formulation based on the Fast Fourier Transform (VPFFT code; *Lebensohn* [2001]; *Lebensohn et al.* [2008]) and ELLE modules to simulate recovery [*Borthwick et al.*, 2014]. ELLE has been successfully used to model a range of coupled microstructural processes, such as static grain growth, strain localization, dynamic

recrystallization, rotation of rigid objects in anisotropic rocks and coupled deformation and recrystallization of polar ice [e.g., *Griera et al.*, 2011; *Griera et al.*, 2013; *Llorens et al.*, 2016a; *Llorens et al.*, 2016b; *Llorens et al.*, 2017; *Steinbach et al.*, 2017, and references thereof]. The last four of these studies made use of the coupled VPFFT/ELLE approach that it is utilized for our simulations. This method allows simulating deformation of a polycrystalline aggregate by dislocation creep and dynamic recrystallization up to high strains, similar to those observed in nature.

The VPFFT code calculates lattice rotations associated with viscoplastic deformation. From these data, recrystallization processes such as grain boundary migration, new grain nucleation or intracrystalline recovery can be simulated using ELLE processes (see descriptions below). In the present study, only the process of recovery is considered, while grain boundary migration, new grain nucleation and grain boundary sliding are deliberately not incorporated. This contribution therefore aims to study the process of subgrain rotation recrystallization in isolation, prior to its coupling with other recrystallization processes in future studies. Our simulations thus cover the idealized regime II (rotational-recrystallization dominated) of *Hirth and Tullis* [1992]. This is coherent with results from pure-halite deformation experiments under dry conditions and relatively low temperatures (lower than 200°C), where the three last processes are not active [*Urai et al.*, 2008]. We therefore concentrate on the analysis of the competition between (i) grain size reduction caused by dislocation creep and (ii) subgrain coarsening by coalescence through rotation and alignment of the lattices of neighboring subgrains (SGC), associated with intracrystalline recovery. The recovery (SGC) process reduces subgrain misorientations associated with the decrease of free energy (i.e., boundary and stored strain energies), thus producing coarsening and coalescence of subgrains that compensate grain size reduction associated with dislocation creep.

2.1 VPFFT – Viscoplastic deformation

In this section we provide a brief summary of the VPFFT approach. A more detailed explanation of the code and how it is implemented can be found in *Lebensohn* [2001] and *Lebensohn et al.* [2008]. This FFT-based code is a full-field formulation that provides a solution of the micromechanical problem by finding a stress and strain-rate field that minimizes the average local work rate under the compatibility and equilibrium constraints (see *Lebensohn* [2001]). In this full-field approach, lattice orientations are mapped on a rectangular grid of Fourier points or unconnected nodes (*unodes*) that represent small material elements and that are also used to store local stress, strain rate and dislocation densities. Lattice rotations due to plastic deformation by dislocation slip are calculated from the velocity gradient and stress fields. The local mechanical response of a non-linear heterogeneous material can be calculated as a convolution integral between Green functions associated with a linear homogenous medium and a polarization field containing all the information on the heterogeneity and nonlinearity of the material's behavior. For periodic media, the Fourier transform allows converting convolution integrals in real space to simple products in the Fourier space. Therefore, the FFTs are used to transform the polarization field into Fourier space, and thus get the mechanical fields by transforming the convolution product back to real space. Since the polarization depend on the unknown mechanical fields, an iterative method is used to obtain a compatible strain-rate field and a stress field in equilibrium related by the constitutive equation.

The viscoplastic behavior of polycrystals is defined using a non-linear viscous rate-dependent model, where deformation is assumed to be accommodated by dislocation glide [*Lebensohn*, 2001] along a number of pre-defined slip systems. The constitutive equation between the strain rate $\dot{\varepsilon}_{ij}(\mathbf{x})$ and the deviatoric stress $\sigma'(\mathbf{x})$ is given by:

$$\dot{\varepsilon}_{ij}(x) = \sum_{s=1}^{N_s} m_{ij}^{s}(x)\dot{\gamma}^{s}(x) = \dot{\gamma}_0 \sum_{s=1}^{N_s} m_{ij}^{s}(x) \left|\frac{m^{s}(x):\sigma'(x)}{\tau^{s}(x)}\right|^{q} sgn\left(m^{s}(x):\sigma'(x)\right), \quad (1)$$

where m^s, $\dot{\gamma}^s$ and τ^s are the symmetric Schmid tensor, the shear strain rate and the critical resolved shear stress defined for the slip system s, respectively. $\dot{\gamma}_0$ is the reference strain rate, q is the rate sensitivity exponent and N_s is the number of slip systems in the crystal.

Once the iteration converges, the microstructure is updated using an explicit scheme assuming that the mechanical fields are constant during a small time increment Δt. The new position of a point $\mathbf{x}$ of the Fourier grid is determined using the velocity fluctuation term $\tilde{v}_i(\mathbf{x})$ (Eq. 25 in *Lebensohn* [2001]) arising from the heterogeneity field as

$$X_i(\mathbf{x}) = x_i^0 + \left(\dot{E_{ij}} x_j^0 + \tilde{v}_i(\mathbf{x})\right) \times \Delta t, \quad (2)$$

where $\dot{E_{ij}}$ is the macroscopic strain rate. The local crystallographic orientations are updated according to the following local lattice rotation

$$\omega_{ij}(\boldsymbol{x}) = \left(\dot{\Omega}(\boldsymbol{x}) + \widetilde{\omega}(\boldsymbol{x}) - \dot{\omega_{ij}^{p}}(\boldsymbol{x})\right) \times \Delta t, \quad (3)$$

where $\dot{\Omega}(\boldsymbol{x})$ is the average rotation rate of the macroscopic velocity gradient tensor, $\widetilde{\omega}(\boldsymbol{x})$ is the local fluctuation in the rotation-rate obtained by taking the antisymmetric part of the velocity gradient fluctuation term $\tilde{v}_{i,j}(\mathbf{x})$, and finally the last term $\dot{\omega_{ij}^{p}}(\boldsymbol{x})$ is the plastic rotation-rate of the crystal lattice that it is calculated as $\sum_{s=1}^{N_s} \alpha_{ij}^{s}(\boldsymbol{x})\dot{\gamma}^{s}(\boldsymbol{x})$,where α_{ij}^{s} is the anti-symmetric Schmid tensor. Lattice misorientations between neighboring Fourier points form where rotation gradients develop, as a consequence of the formation of deformation gradients. As such, high subgrain misorientations develop in areas of high strain gradients. After VPFFT induces lattice rotations, and before the intracrystalline recovery process, a routine checks if the local misorientation exceeds the local misorientation angle that defines a high-angle grain boundary (HAGB). A new HAGB is thus created when misorientation exceeds 15°. This results in the formation of recrystallized, new grains, and hence in grain size reduction. Grains in the model are defined by nodes that are connected by straight grain-boundary segments, and therefore named boundary nodes (*bnodes*). As grain boundary migration [e.g., *Piazolo et al.*, 2002; *Llorens et al.*, 2016a; *Llorens et al.*, 2016b; *Llorens et al.*, 2017] is disabled in this study, the only role of HAGBs is to restrict recovery and subgrain-boundary formation within individual grains. *Bnodes* are displaced by deformation according to Eq. (2).

2.2 ELLE – Intracrystalline recovery

After each deformation step, the new microstructure configuration provided by the VPFFT calculation is used by the ELLE-recovery module that simulates intracrystalline recovery

that is driven by a reduction of the local misorientation generated by dislocations, following a modification of the method of *Borthwick et al.* [2014] and *Llorens et al.* [2016a] (see Supporting Information for a full description of the method). Lattice-orientation heterogeneities are reduced by local rotation of the lattice without moving high-angle grain boundaries (HAGB). The recovery routine simulates annihilation of dislocations and their rearrangement into low-angle subgrain boundaries (i.e., polygonization; *Urai et al.* [1986]) and the development of areas with homogenous crystal orientations by coalescence through rotation and alignment of the lattices of neighboring subgrains.

The smallest region with a homogenous lattice orientation in the model is a *unode* (unconnected node), which is treated as a subgrain or crystallite. Geometrical necessary dislocations arise from orientation differences between the lattices in adjacent *unodes*. Rotation of the lattice in one single *unode* changes these orientation differences and, hence, the local dislocation density and associated energy. Since all geometrically necessary dislocations are located at the boundaries between *unodes*, their energy can be treated as a boundary energy that is a function of orientation difference between *unodes*. The recovery routine essentially calculates and applies small increments of lattice orientation in individual *unodes* that is driven by the associated dislocation energy reduction. The model assumes that the rotation rate of a crystallite/subgrain is proportional to the torque (Q) generated by the change of surface energy associated with the misorientation reduction [*Randle*, 1993]. A linear relation between the angular velocity ω and a driving torque Q is assumed

$$\omega = M'Q \tag{4}$$

where *M'* is the rotational mobility [*Moldovan et al.*, 2002]. Considering a 2D microstructure, the torque acting on a crystallite delimited by n subgrain boundaries (sb) is given by

$$Q = \sum_n l_{sb}\, d\gamma_{sb}/d\theta_{sb} \tag{5}$$

where l_{sb} denotes the boundary length with grain boundary energy γ_{sb} and misorientation angle θ_{sb} across the boundary between the reference subgrain and a neighboring subgrain sb. In the model, each crystallite (*unode*) is regarded as a small, square (potential) subgrain. For low-angle boundaries, the boundary energy is calculated as a function of the misorientation angle with the Read-Shockley equation [*Read and Shockley*, 1950]. For such misorientation angles, the equivalent rotations by crystal symmetry are considered in order to obtain the minimum misorientation θ between two crystallites or *unodes* (i.e., disorientation). In the original model by *Moldovan et al.* [2001; 2002], the rotation mobility *M'* was expressed as function of boundary and/or lattice self-diffusion. Here, our approach differs from the original one because we have assumed that *unode* (crystallite) lattice rotation is accommodated by cooperative motion/rearrangement of boundary dislocations (*Li* [1962]), by reducing the local misorientation. Since we assume rigid rotation of square *unodes*, a mechanism of boundary and lattice diffusion is required in order to keep areas constant along their edges. Due to the lack of experimental data, and as a first approach, we assume that subgrain rotation can be described as a linear viscous process where *M'* is expressed as function of the effective viscosity of the material η (see Supporting Information for the full description). For a square shape this relationship is

$$M' = \frac{1}{8\eta}\frac{1}{d^2} \tag{7}$$

where d is the subgrain size (i.e., one *unode*).

The recovery process in ELLE assumes that each *unode* is a potential subgrain and thus the boundary energy and misorientation is minimized by the rotation of each *unode*. The algorithm starts by choosing a random *unode* and finding the first-neighboring *unodes* that belong to the same grain. The crystal orientation of the reference *unode* is rotated towards the value that results in the maximum reduction in energy calculated from systematic trial rotations, being the crystal orientation unchanged if all trial positions result in an increase of energy of the neighborhood. This procedure is repeated for each *unode* in random order every time step. The numerical predictions were verified by *Borthwick et al.* [2014] using results from intracrystalline evolution during annealing experiments of deformed single salt crystals. Our method presents some slight differences with that of *Borthwick et al.* [2014]. These are that: (i) rotation in our approach depends on the boundary energy reduction and (ii) we use a direct relationship between M' and the material properties based on the material's effective viscosity (see Supporting Information for more details). An alternative way to constrain M' could be based on the use of misorientation decay during annealing experiments. Although there is data from high-temperature halite experiments [e.g., *Borthwick et al.* 2012 and references therein], there is certainly no published data for halite deformed in the low-temperature regime. Therefore, the approach taken is the most appropriate for estimating M' values. A comparison of the kinetics of recovery calculated from annealing experiments versus those using our approach is discussed in the Supporting Information and Fig. S1.

2.3 Experimental setup and postprocessing

An initial microstructure composed of 255 grains is discretized into a resolution of 256x256 Fourier points (or *unodes*), resulting in a unit cell formed by 65,536 nodes**.** These nodes provide the physical properties within grains and store the lattice orientation, defined with the three Euler angles. A set of random initial orientations (Figure 1) was assigned to the initial grains, and the initial crystal preferred orientation (CPO) results in near isotropic bulk behavior. The data structure on VPFFT/ELLE is fully periodic, in a way that grains reaching one side of the model continue on the other side. The initial model is a 1x1 cm square and, therefore, the *unode* distance is set to d=1/256 cm. Every deformation time step all the parts of the model outside the square unit cell are repositioned back into it. This improves the visualization of the microstructures, even when high shear strains are reached. In ELLE, each process is simulated as a separate module that acts on the data structure [*Jessell et al.*, 2001]. The program flow and coupling between the viscoplastic VPFFT code and ELLE are similar to those used by *Griera et al.* [2011], *Griera et al.* [2013], *Llorens et al.* [2016a], *Llorens et al.* [2016b], *Llorens et al.* [2017] and *Steinbach et al.* [2017]. Each process is activated sequentially in a loop that represents a small increment $\Delta\gamma$ of viscoplastic deformation calculated with VPFFT followed by recovery during a small time increment Δt. Since an elastic component is not incorporated in our models, the mechanical response of the viscoplastic model only depends on the current configuration. Moreover, the same operator-splitting procedure of coupling processes sequentially has been successfully used in a number of viscous and viscoplastic numerical simulation studies utilizing the ELLE platform (see *Piazolo et al.* [2002], *Bons et al.*, [2008], *Jessell et al.* [2009], *Griera et al.* [2013], *Llorens et al.* [2013], *Llorens et al.* [2017], *Steinbach et al.* [2016] and references thereof), and tested for our specific model configuration (see below).

The constitutive behavior of halite polycrystals is simulated using a system with cubic symmetry where deformation is accommodated by three sets of slip systems: $\{110\}\langle\bar{1}10\rangle$, $\{100\}\langle011\rangle$ and $\{111\}\langle\bar{1}10\rangle$ [e.g., *Carter and Heard*, 1970]. In this approach, the resistance of slip systems to glide is defined by a critical resolved shear stress (τ^s). The degree of anisotropy (A) is set as the ratio between the critical resolved shear stress with respect to the easiest glide system, which is $\{110\}\langle\bar{1}10\rangle$ for halite at low temperature. Following single crystal experiments by *Carter and Heard* [1970], we have set CRSS as three times higher for the $\{100\}\langle011\rangle$ slip system (i.e., A=3), and two times for the $\{111\}\langle\bar{1}10\rangle$ system (i.e., A=2). The stress exponent is set to q=7 for all the experiments. From a mechanical point of view, the VPFFT approach assumes that the CRSS' do not change throughout time (i.e., there is no hardening associated with interaction of dislocations), and therefore these A values are kept constant throughout the simulation. Experimental observations indicate that climb of dislocations is not active in halite at the simulated range of temperatures [e.g., *Borthwick and Piazolo*, 2010], hence hardening of CRSS (e.g., by cross slip) associated with strong interaction between slip systems is not expected here.

Dextral simple-shear deformation was modeled in increments of $\Delta\gamma$=0.04 up to γ=4, although significantly higher shear strains can be achieved at the cost of calculation time. Four different recovery scenarios were modeled by varying the number of computational steps of the recovery (SGC) process per deformation step: SGC0, SGC1, SGC10 and SGC25. A constant time step of $2x10^8$ s (~6 years) was used for all simulations and, therefore, the shear strain rate was $2x10^{-10}$ s^{-1}. There are no experimental data to constrain the rotation mobility M' parameter used in the recovery models. The M' value was calculated with equation (7), taking a reference viscosity of $5x10^{16}$ Pa·s (model SGC1). This value was determined from flow laws derived from halite experiments for the given strain rate (after *Urai et al.* [2008]), assuming a low temperature (< 50 ºC) and for our strain rate. As the strain rate is constant for all models, an increase of the number of recovery steps implies a reduction of the effective viscosity. We interpret this reduction as associated with a temperature increase that causes a higher activity of recrystallization processes. For the SSG10 and SSG25 simulations the estimated viscosities are $5x10^{15}$ Pa·s and $2x10^{15}$ Pa·s, respectively. This range of calculated values is in agreement with bulk viscosities observed from halite deformation experiments for the aforementioned low temperature conditions [*Urai et al.*, 2008]. For the model without recovery (SGC0), the rotation mobility is assumed to be sufficiently small not to produce microstructure modifications for the time and length scale of our simulations. The viscosity of this model should be at least higher than that of the reference model SGC1.

The numerical results were post-processed using the texture calculation toolbox MTEX (http://mtex.googlecode.com; *Bachmann et al.* [2010], *Mainprice et al.* [2011]). MTEX allows generating maps (i.e., lattice orientation, misorientation boundaries) and analyzing the CPOs in a similar way as for EBSD data of natural or experimental samples, thus allowing a direct comparison of 2D sections.

A series of simulations based on the model SGC10 were analyzed in order to investigate the influence of the time step size on the resulting microstructures. For this purpose, we ran models with incremental shear strains of $\Delta\gamma$=0.008, 0.016, 0.024, 0.032, 0.04, 0.08, 0.12 and 0.16, keeping the same balance of subgrain coarsening with respect to shearing. This means that

runs with a larger shear strain increment underwent a higher number of recovery (SGC) steps. The results are summarized in Figure S2 (Supporting Information) and demonstrate that the chosen time step size has a very limited influence on the results. This difference is associated with the fact that relatively high misorientations are reduced in the first step of the SGC process. We chose to run the models with a shear strain increment of Δ_{inc}=0.04 per time step as a compromise between accuracy and simulation time. The difference between this base model and that with very small time steps is very small, with a variation of less than 0.2° of the mean misorientation of the model (Figure S2).

3 Results

Orientation maps resulting from the simulations without recovery (SSG0) show a microstructure with strong grain size reduction and increasing elongation of relict grains (defined by the original grain boundaries) with progressive deformation (Figure 2; Movie ms01 of the SGC0 model in additional supporting information). These processes become extreme at relatively high shear strains, where only a few large relict grains immersed in a recrystallized matrix are recognizable (e.g., Figure 2d at γ=4). It is worth noting that the term recrystallized matrix here refers to areas of small grains formed by rotation recrystallization (i.e., by the so called grain refinement process in metallurgical and material science). As expected, the angle between the developing foliation and the shear plane progressively reduces with increasing strain, although at γ=4 the foliation is still oblique to the shear plane. Relict grains tend to show a shape-preferred orientation oblique to the shear plane and coherent with the imposed dextral shear sense. Deformation is distributed along the polycrystal, and no localization bands in areas with preferred grain size reduction can be distinguished. With increasing shear strain, grain orientations trend towards acquiring {110} orientations parallel to the shear direction (i.e., green tones in Figure 2), while very few grains with {111} parallel to the shear direction (i.e., blue tones in Figure 2) can be found.

Grains deform internally in a different way depending on their initial geometry and orientation and those of their neighbors. For example, at relatively low strains (γ=1) some grains develop a network of subgrains (Figure 2b), while others have homogeneous crystal orientations or smooth orientation gradients without distinct subgrain boundaries. The first detectable low-angle grain boundaries (LAGB; smaller than 15º) tend to form next to triple nodes, because orientation differences between grains in these areas tend to result in strain incompatibility and therefore lead to the activation of different slip systems. Some of these LAGBs subsequently develop into high-angle grain boundaries (HAGB; higher than 15º) to form new and smaller grains, which display a parent and daughter grain structure between relict and recrystallized grains (i.e., formed by rotation recrystallization). Areas with recrystallized grains tend to be initially isolated, surrounding parental grains. With progressive strain these areas tend to join and form connected bands that finally result in a continuous matrix at higher strain. At relatively low strains (γ=1) new grains formed by rotation recrystallization tend to be grouped in clusters. Grains with denser subgrain networks have a tendency to have {100} close to the shear direction (red tones in Figure 2). The orientation of subgrain boundaries in banded grains generally varies between the direction of the grain elongation or foliation and the shear plane. Subgrain rotation significantly increases with progressive strain, causing a strong grain size reduction in the SGC0 model.

Simulations that include intracrystalline recovery show that subgrain coarsening and coalescence significantly reduce subgrain misorientations and therefore the density of subgrain boundaries. Thus, the intensity of grain size reduction is significantly lower in those models, allowing the survival of larger grains and subgrains with progressive deformation (Figure 3; Movie ms02 of the SGC0 model in additional supporting information). Crystal preferred orientations (CPOs) are qualitatively not changed when there is recovery, but their intensity is enhanced (Figs. 3, 4). Subgrain-free grains dominate in simulations with strong recovery (SGC10 or SGC25; Figure 3g-l), with many grains having internal misorientations lower than 5º. Orientation maps of the deviation of individual *unodes* or crystallites with respect to the mean orientation of the grain help to highlight the subgrain structure (Figure 3c,f,i,l). Strong subgrain size reduction with significant deviations from the mean orientation of the grains can be seen in simulations with low or no recovery (SGC1 or SGC0). However, increasing recovery strongly reduces these deviations and the map shows clearer (white) areas, meaning that the misorientation of crystallites with respect to the grain mean is very low.

A close look at the grains better reveals the effects of recovery. For example, Figure 5 shows details of three selected grains (indicated in Figure 1), comparing the experiment without recovery (SGC0) with that with 10 steps of recovery per deformation step (SGC10). The increase of recovery reduces the spread of orientations and decreases subgrain boundary misorientations. The results illustrate how two grains with relatively similar initial orientations (A and B) develop different lattice orientation distributions after a shear strain of one. Three subgrains with very different orientations develop in grain A. The new grain limits are subparallel to the shear plane. Contrary to this, grain B develops banded subgrains, with alternating orientations. The new grain boundaries within this grain are oriented parallel to its elongation direction. Grain C shows the same orientations in both cases, although there are more subgrain boundaries in the model without recovery (SGC0). For the three cases, subgrain boundaries are sub-parallel to a direction of the {110} planes. There is a maximum clustering of axes parallel to the <100> direction (i.e., parallel to the normal of the intermediate strain axis of simple shear deformation). On the contrary, the other axes are more dispersed. This indicates that the misorientation axes for this type of boundaries is <100> and corresponds to a tilted boundary, as this axis is included in the boundary plane.

Stereograms reveal that crystal orientation poles are oriented almost identical for the whole series of experiments, but there is more scattering and a less intense CPO in the models with limited or no recovery. At all stages of deformation, orientations are spread, as indicated by orientation maps (Figs. 2,3) and pole figures (Figure 4). Despite the scattered distribution, the {110} and {111} pole figures at γ=1 already display a weak hexagonal symmetry, both in models with and without recovery. On the contrary, the {100} stereogram shows a more asymmetric pattern, which evolves with progressive deformation towards a pattern with a maximum perpendicular to the shear plane and two maxima at 45º to it. At γ=4 there are two {110} maxima parallel and perpendicular to the shear plane, respectively, plus another four maxima at 45º of it. Four {111} maxima form at 45º to the shear direction. Orientations in individual grains display a wide distribution with a similar symmetry to that of the bulk, although they can appear rotated depending on the initial orientation of the selected grain and its neighbors (Figure 4).

The analysis of the slip system activity reveals that all the sets of pre-defined slip systems all contribute to deformation (Figs. 6, 7). In all our simulations, nearly 50% of strain is

accommodated, on average, by the {111} systems. At the onset of deformation, when grain distribution is random, 48% of strain is accommodated by these systems, 34% by the easiest glide {110} system, and 18% by the hardest {100} systems. In order to check the consistency of these values, the SGC0 simulation was repeated ten times with different initial grain orientations, and the maximum deviation of bulk activities at γ=1 was ±0.4%. With increasing strain, the activity of {111} systems remains approximately constant, while that of the {110} system slightly decreases and {100} increases. At γ=4, and for the model without subgrain coarsening, 29% of strain is accommodated by the {110} system and 24% by {100}. When there is recovery, the activity of {111} system remains similar but the activity balance between the hardest and easiest slip systems slightly changes throughout the experiment, although the activity of the {110} system is always higher than that of the {100} (Figure 6d at γ=4). Maps displaying the distribution of slip system activity show that the {111} systems dominate and widely affect the whole sample (pale tones in Figure 7). The relative activity of the second slip system, either {110} (blue) or {100} (red), determines the evolution of each grain. Some grains, such as those marked with A, B and C, start displaying banded regions with differences in slip system activity from the onset of deformation (Figure 7a), thus giving rise to subgrains that evolve to form new grains with increasing strain. In some cases, subgrains can form even if the same slip systems dominate, but they have different activities. The subgrains developed in the lower part of grain A, which are all determined by {100} systems, are a good example of this phenomenon (Figs. 5 and 7b). The slip system activity maps are relatively similar in models with and without recovery. For the three selected grains of Figure 5, subgrain boundaries are formed as consequence of differences in the activation of the {110} and {100} sets between subgrains.

The frequency distribution of geometric mean misorientations of initial individual grains is shown in Figure 8. At the onset of deformation, subgrain boundaries showed low mean misorientations, which rapidly increased and spread with progressive deformation. However, the rate of this increase slows down at relatively high strains. The distribution of mean values for individual grains is close to exponential at the beginning of deformation, but becomes closer to normal at higher strains (e.g., at γ=2-4) for the models without recovery (SGC0). When subgrain coarsening is active (in models with SGC>0), mean misorientation values are significantly lower, although their spread is similar to the cases without SGC. Values at higher strains tend to deviate from a normal distribution with increasing SGC.

4 Discussion

The main objectives of this study are (i) to investigate the microstructural evolution of halite polycrystals during simple shear deformation with subgrain rotation recrystallization, and (ii) to assess the use of subgrain misorientations as a strain gauge in polycrystals that undergo different intensities of intracrystalline recovery. We specifically simulate halite deformation and recrystallization under dry conditions and at relatively low temperatures, focusing on the competition between (i) grain size reduction by subgrain rotation induced by dislocation creep and (ii) subgrain coarsening driven by the reduction of local misorientation associated with intracrystalline recovery. Our simple-shear simulations produce qualitatively similar results to those from halite deformation experiments by other authors, validating the proposed numerical approach. Specifically, our numerical microstructures (Figs. 2, 3, 5) and CPOs (Figure 4) can be directly compared with the published torsion experiments of dry halite at 100 and 200 °C by *Armann* [2008] and *Wenk et al.* [2009]. Our calculated values of mean misorientation and

subgrain misorientation statistics are qualitatively similar to those obtained with EBSD by *Pennock et al.* [2005] for dry halite deformed in coaxial conditions at 165±10ºC.

The experiment without recovery (SGC0) very well illustrates the process of grain size reduction, with the formation of LAGBs that evolve to HAGBs. Subgrains start forming at the early stages of deformation, as in other materials [e.g., *Hurley and Humphreys*, 2003]. Subgrain formation and the development of subgrain misorientations do not only depend on the initial grain orientation, but also on the relative orientations of the surrounding grains. This was also observed in experiments by *Pennock et al.* [2005]. The SGC0 simulation reproduces very similar CPOs as those with the VPSC approach [e.g., *Wenk et al.*, 2009], in which only deformation by dislocation glide is taken into account. In this situation, there is a strong grain size reduction (see evolution of number of grains in Fig. 8a-e), but there are a few relict grains that can survive throughout deformation, depending on their initial orientation and that of their neighbors. As expected, grain elongation increases and rotates towards the shear plane with increasing strain. Orientation maps show a wide distribution, although grains with {110} orientations parallel to the shear direction dominate. The predicted CPOs also reproduce those from low-temperature halite experiments by *Armann* [2008] and *Wenk et al.* [2009] well, although our simulations produce less scattering. This is probably due to the complete absence of other recrystallization processes or deformation mechanisms in the simulations. The addition of recovery changes the deformational behavior of the samples, since subgrain recrystallization associated with the reduction of stored strain and boundary energies significantly decreases grain size reduction (values displayed in Fig. 8), especially in the experiments SGC10 and SGC25. This process does not change CPOs, but results in a more homogeneous microstructure. As indicated in section 2.3, the increase of recovery is simulated with the assumption of a reduction of the effective viscosity of the material, allowing more rotation at the same driving force. Since viscosity is temperature-dependent, this effect would be linked to a temperature increment in natural cases [*Borthwick and Piazolo*, 2010].

A detailed analysis of the slip system activity reveals that the three sets of slip systems all contribute to accommodation of strain, with the {111} systems the most active through time in all numerical experiments. This result is consistent with the VPSC simulations of *Wenk et al.* [2009] after their models reached a relatively stable slip system activity (at γ~3.5). This predominance can be explained because there are twelve {111} slip systems, and only six of the other two sets ({110} and {100}). Contrarily to VPSC models, the weakest {110} slip systems dominate over the hardest {100} ones in our simulations. However, this difference varies with progressive strain and is not very marked (Figure 6). Moreover, our results show how subgrain coarsening associated with recovery can also slightly modify the distribution of slip system activity, in addition to non-coaxial flow, making the use of texture patterns to determine slip system activity more complex in such systems. Maps of slip system activity support this observation (Figure 7).

In principle, subgrain misorientations can be used as a strain gauge for dislocation creep deformation in crystalline materials, if we can determine how the misorientation angles correlate with strain [e.g., *Pennock et al.*, 2004; 2005]. This tool can be especially useful for structural analysis in areas where there is a recognizable strain gradient. Over the past 15 years, EBSD mapping has allowed the collection of large misorientation datasets in materials such as metals or halite [e.g., *Randle and Enger*, 2000; *Humphreys*, 2001; *Pennock et al.*, 2002; 2005; 2006;

Hurley and Humphreys, 2003; *Pennock and Drury*, 2005, among others]. As discussed in the introduction, a power law relationship of the average subgrain boundary misorientation of the whole sample (θ_{av}) and natural strain (ε) can be found, and this scaling relationship seems to be universal [e.g., *Hughes et al.*, 1997; 1998; 2003; *Pantleon*, 1997; 1998; 2001; *Sethna and Coffman*, 2003]. These studies propose that $\theta_{av} \sim \varepsilon^{n=2/3}$ for geometrically necessary boundaries (GBN's).

Pennock and Drury [2005] measured n=0.41 in halite pure shear experiments, while *Pennock et al.* [2005] obtained n=0.42 when using the average subgrain misorientations within grains ($\theta_{av,grains}$), instead of the whole sample:

$$\theta_{av\text{-}grains} = k_1 \, \varepsilon^n \tag{8}$$

where k_1 is a constant, with a value of 3.3° for their experiments. Our subgrain-misorientation data measured on a grain basis closely follow the universal exponent of n=2/3 (Figure 9). Note that here we use the geometric mean instead of the average, since this is a more appropriate parameter given that misorientations distributions are frequently non-Gaussian (Figure 8). Moreover, we prefer to calculate a weighted geometric mean, in a way that the contribution of each grain to the mean depends on their number of crystallites. We find that the k_1 constant depends on the intensity of recovery (SGC), and hence on temperature, and k_1 decreases from 4.82° for SGC0 to 0.72° for SGC25 (see list of values in Figure 9). Since only the models with recovery can be scaled, k_1 appears capped at about 4.82° for the model SGC0. The applicability of this law is limited at the other end of the range by the rate where grain boundary migration becomes a significant factor for the subgrain structure. It is important to note that the scaling law is not the best power law fit of the simulation data (Figure 9). With increasing recovery, the best fit exponent decreases from n=0.81 for SGC0 to 0.53 for SGC25. However, the coefficients of determination R^2 between these data and the predicted values are high (Figure 9), and therefore the proposed law provides a good approximation. Our results demonstrate that recovery influences the exponent of the scaling law and can help to interpret the low n values obtained by *Pennock and Drury* [2005; 2006] (n=0.41-0.42). This low exponent can be related to the activation of intracrystalline recrystallization processes during those deformation experiments, leading to a decrease of intracrystalline heterogeneities and a reduction of n. Our simulations show how the mean subgrain misorientations within grains can be used as a strain gauge in materials undergoing intracrystalline recovery, not only in coaxial deformation conditions but also in simple shear up to high strain. The values obtained confirm that the universal exponent proposed above applies to halite, at least when it is deformed in the absence of grain boundary migration. Additionally, this strain gauge could be potentially applied to rock that underwent grain boundary migration if grain nuclei keep relatively high misorientations (e.g., as in *Schléder and Urai* [2007]). However, to verify this a whole new study would need to be made. Unfortunately, our misorientation data cannot be compared with those from torsion (simple shear) halite experiments, since *Armann* [2008] or *Wenk et al.* [2009] did not provide quantifications of misorientation.

The models presented in this contribution reproduce the behavior of dry halite deformed at low temperatures (<200 °C) well. This type of simulations may not only be key for understanding halite rheology, but also that of other minerals with similar symmetry and slip systems. For example, magnesiowüstite deforms plastically in the lower mantle, where it is one

583 of the two major phases, potentially resulting in strain weakening and localized deformation
584 [*Girard et al.*, 2016]. Full-field simulations such as the ones presented here, can provide new
585 insights into the interplay of deformation mechanisms and resulting flow laws in the mantle, thus
586 improving our understanding of Earth's dynamics.

587 **5 Conclusions**

588 We presented a new method to model subgrain rotation recrystallization in
589 polycrystalline aggregates, and applied it to dry halite. The analysis of the resulting
590 microstructures led to the following main conclusions:

591 • The VPFFT/ELLE numerical approach presented in this contribution accurately
592 reproduces experimental microstructures, allowing the systematic analysis of systems in
593 which multiple deformation processes are active. This full-field method has been applied
594 to halite for first time, providing new insights into the competition between (i) grain size
595 reduction by dislocation creep and (ii) subgrain coarsening by coalescence through
596 rotation and alignment of the lattices of neighboring subgrains, associated with
597 intracrystalline recovery.

598 • Viscoplastic deformation results in the development of low-angle grain boundaries that
599 evolve to form high-angle grain boundaries, leading to a strong grain size reduction. The
600 activation of subgrain coarsening associated with the decrease of strain stored energy by
601 recovery significantly decreases grain size reduction, although grain orientations are
602 similar in all cases.

603 • Subgrain coarsening does not significantly modify crystal preferred orientations, but
604 results in less scattered crystal orientations.

605 • All the sets of pre-defined slip systems contribute to deformation, with changes in their
606 relative activity depending on progressive strain and the amount of subgrain coarsening.
607 These results are in accordance with published laboratory experiments and viscoplastic
608 self-consistent simulations.

609 • Mean subgrain misorientations per grain can be used as a strain gauge in systems with
610 different degrees of subgrain rotation recrystallization, with a universal scaling exponent
611 of $n \sim 2/3$ that accounts for all cases. The intensity of intracrystalline recovery, and hence
612 temperature, can potentially be estimated with this strain gauge if misorientations can be
613 measured in an area with a strain gradient. This type of strain gauge can be further
614 developed and refined for different geological materials if misorientation data from
615 experiments and field studies are available for comparison with simulations.

616 **Acknowledgments and Data**

617 We thank the Microdynamics of Ice (Micro-DICE) research network, funded by the
618 European Science Foundation (ESF), for providing two short visit grants to EGR and AG that
619 allowed carrying out the numerical experiments. EGR also acknowledges a mobility award
620 funded by the Santander Universities network. The series of simulations were run using the
621 Maxwell High Performance Computer Cluster of the University of Aberdeen. Supporting

622 information accompanies this paper, including (i) a detailed explanation of the approach taken to
623 simulate intracrystalline recovery, (ii) a figure that analyzes the influence of the time step size in
624 the numerical results and (iii) two simulation movies. The codes are open source and available at
625 http://www.elle.ws. Correspondence and requests for materials should be addressed to Enrique
626 Gomez-Rivas. We gratefully acknowledge three anonymous reviewers, whose constructive
627 reviews greatly improved the manuscript, together with the editorial guidance of Yoshihiro
628 Kaneko and Paul Tregoning.

629 **References**

630 Armann, M. (2008), Microstructural and textural development in synthetic rocksalt deformed in
631 torsion. PhD Thesis, ETH-Zürich, Switzerland.

632 Ashby, M. F. (1970), The deformation of plastically non-homogeneous materials. Philos. Mag.
633 21, 399-424.

634 Bachmann, F., R. Hielscher, and H. Schaeben (2010), Texture analysis with MTEX - free and
635 open source software toolbox. Solid State Phenom. 160, 63-68.

636 Bons, P.D., D., Koehn, M.W. Jessell (Eds.), (2008), Microdynamic Simulation. Lecture Notes in
637 Earth Sciences 106, Springer, Berlin, 405 pp.

638 Borthwick, V. E., and S. Piazolo (2010), Complex temperature dependent behaviour revealed by
639 in-situ heating experiments on single crystals of deformed halite: New ways to recognize
640 and evaluate annealing in geological materials. J. Struct. Geol. 32, 982-996.

641 Borthwick, V.E., S. Piazolo, S. Schmidt, C. Gundlach, A. Griera, P.D. Bons, and M.W. Jessell,
642 (2012), The application of in situ 3D X-ray diffraction in annealing experiments: first
643 interpretation of substructure development in deformed NaCl. Mater. Sci. Forum 715-
644 716: 461-466.

645 Borthwick, V. E., S. Piazolo, L. Evans, A. Griera, and P. D. Bons (2014), What happens to
646 deformed rocks after deformation? A refined model for recovery based on numerical
647 simulations. Geol. Soc. London Spec. Publ. 394(1), 215-534.

648 Bunge, H. J. (1985), Representation of preferred orientations. In: Weiss, L. E., Wenk, H. R.
649 (Eds.), Preferred orientation in deformed metals: an introduction to modern texture
650 analysis. Academic Press, London, 73-104.

651 Carter, N. L., and H. C. Heard (1970), Temperature and rate dependent deformation of halite.
652 Am. J. Sci. 269, 193-249.

653 Erb, U., and H. Gleiter (1979), The effect of temperature on the energy and structure of grain
654 boundaries. Scripta Metall. 13, 61-64.

655 Farla, R. J. M., H. Kokkonen, J. D. Fitz Gerald, A. Barnhoorn, U. H. Faul and I. Jackson (2010),
656 Dislocation recovery in fine-grained polycrystalline olivine. Phys Chem Minerals, DOI
657 10.1007/s00269-010-0410-3.

658 Girard, J., G. Amulele, R. Farla, A. Mohiuddin, and S. Karato (2016), Shear deformation of
659 bridgmanite and magnesiowüstite aggregates at lower mantle conditions. Science
660 351(6269):144-7.

661 Griera, A., P. D. Bons, M. W. Jessell, R. Lebensohn, L. Evans, and E. Gomez-Rivas (2011),
662 Strain localization and porphyroclast rotation. Geology 39, 275-278.

663 Griera, A., M. -G. Llorens, E. Gomez-Rivas, P. D. Bons, M. W. Jessell, L. A. Evans, and R.
664 Lebensohn (2013), Numerical modelling of porphyroclast and porphyroblast rotation in
665 anisotropic rocks. Tectonophysics 587, 4-29.

666 Guillope, M., and J. P. Poirier (1979), Dynamic recrystallization during creep of single-
667 crystalline halite: an experimental study. J. Geophys. Res. 84, 5557-5567.

668 Halfpenny, A., D. J. Prior, and J. Wheeler (2006), Analysis of dynamic recrystallization and
669 nucleation in a quartzite mylonite. Tectonophysics 427, 3-14.

670 Hirth, G., and J. Tullis (1992), Dislocation creep regimes in quartz aggregates. J. Struct. Geol 14,
671 145-159.

672 Hughes, D. A., Q. Liu, D. C. Chrzan, and N. Hansen (1997), Scaling of microstructural
673 parameters: misorientations of deformation induced boundaries. Acta Mater. 45, 105-112.

674 Hughes, D. A., D. C. Chrzan, Q. Liu, and N. Hansen (1998), Scaling of misorientation angle
675 distributions. Phys. Rev. Lett. 81, 4664.

676 Hughes, D. A., N. Hansen, and D. J. Bammann (2003), Geometrically necessary boundaries,
677 incidental dislocation boundaries and geometrically necessary dislocations. Scr. Mater.
678 48, 147-153.

679 Humphreys, F. J. (2001), Review: grain and sub-grain characterization by electron backscatter
680 diffraction. J. Mater. Sci. 36, 3833-3854.

681 Humphreys, F. J., and M. Hatherly (2004), Recrystallization and Related Annealing Phenomena,.
682 Third ed. Elsevier Ltd, Oxford.

683 Hurley, P. J., and F.J. Humphreys (2003), The application of EBSD to the study of substructural
684 development in a cold rolled single-phase aluminium alloy. Acta Mater. 51, 1087-1102.

685 Jessell, M.W., P.D. Bons, L. Evans, T. Barr and K. Stüwe (2001), Elle: a micro-process approach
686 to the simulation of microstructures. Comput. Geosci. 27, 17-30.

687 Jessell, M. W., P. D. Bons, A. Griera, L. A. Evans, and C. J. L. Wilson (2009), A tale of two
688 viscosities. J. Struct. Geol. 31, 719-736.

689 Kaminski, E., and N. M. Ribe (2001), A kinematic model for recrystallization and texture
690 development in olivine polycrystals. Earth Planet. Sci. Lett. 189, 253-267.

691 Karato, S. (2012), Deformation of Earth Materials: An Introduction to the Rheology of Solid
692 Earth. Cambridge Univeristy Press. 482 pp.

693 Kuhlmann-Wilsdorf, D., and N. Hansen (1991), Geometrically necessary, incidental and
694 subgrain boundaries. Scr. Mater. 25(7), 1557-1562.

695 Lebensohn, R.A. (2001), N-site modelling of a 3D viscoplastic polycrystal using fast Fourier
696 transform. Acta Mater. 49(14), 2723-2737.

697 Lebensohn, R. A., P. R. Dawson, H. -R. Wenk, and H. M. Kern (2003), Heterogeneous
698 deformation and texture development in halite polycrystals: comparison of different
699 modeling approaches and experimental data. Tectonophysics 370, 287-311.

Lebensohn, R. A., R. Brenner, O. Castelnau, and A. D. Rollett (2008), Orientation image-based micromechanical modelling of subgrain texture evolution in polycrystalline copper. Acta Mater. 56(15), 3914-3926.

Li, J. C. M. (1962), Possibility of subgrain rotation during recrystallization. J. Appl. Phys. 33, 2958-2965.

Llorens, M-.G., P.D. Bons, A. Griera, E. Gomez-Rivas and L.A. Evans (2013), Single layer folding in simple shear. J. Struct. Geol., 50, 209-220.

Llorens, M. -G., A. Griera, P. D. Bons, J. Roessiger, R. Lebensohn, L. A. Evans, and I. Weikusat (2016a), Dynamic recrystallisation of ice aggregates during co-axial viscoplastic deformation: a numerical approach. J. Glaciol. 62(232), 359-377.

Llorens, M. -G., A. Griera, P. D. Bons, R. Lebensohn, L. A. Evans, D. Jansen, and I. Weikusat. (2016b), Full-field predictions of bubble-free ice dynamic recrystallisation under simple shear conditions. Earth Planet. Sci. Lett., 450, 233-242.

Llorens, M. -G., A. Griera, F. Steinbach, P.D. Bons, E. Gomez-Rivas, D. Jansen, R. Lebensohn, and I. Weikusat (2017), Dynamic recrystallisation during deformation of polycrystalline ice: insights from numerical simulations. Phil. Trans. R. Soc. A, 375:20150346.

Mainprice, D., R. Hielscher, and H. Schaeben (2011), Calculating anisotropic physical properties from texture data using the MTEX open source package. Geol. Soc. London Spec. Publ. 360(1), 175-192.

Moldovan, D., D. Wolf, and S. R. Phillpot (2001), Theory of diffusion-accommodated grain rotation in columnar polycrystalline microstructures. Acta Mater. 49(17), 3521-3532.

Moldovan, D., D. Wolf, S. R. Phillpot, and A. J. Haslam (2002), Role of grain rotation during grain growth in a columnar microstructure by mesoscale simulation. Acta Mater. 50(13), 3397-3414.

Pantleon, W. (1997), On the evolution of disorientations in dislocation cell structures during plastic deformation. Mater. Sci. Eng. A234-236, 567-570

Pantleon, W. (1998), On the statistical origin of disorientations in dislocation structures. Acta Mater. 46(2), 451-456.

Pantleon, W. (2001), The evolution of disorientations for several types of boundaries. Mater. Sci. Eng. A319-321, 211-215.

Passchier, C. W., and R. A. J. Trouw (2005), Microtectonics. Springer, Berlin.

Pennock, G. M., and M. R. Drury (2005), Low angle subgrain misorientations in deformed NaCl. J. Microsc. 217, 130-137.

Pennock, G. M., M. R. Drury, P. W. Trimby, and C. J. Spiers (2002), Misorientation distributions in hot deformed NaCl using electron backscattered diffraction. J. Microsc. 205(3), 285-294.

Pennock, G. M., M. R. Drury, and C. J. Spiers (2004), Investigation of subgrain rotation recrystallization in dry polycrystalline NaCl. Mater. Sci. Forum 467-470, 597-602.

738 Pennock, G. M., M R. Drury, and C. J. Spiers (2005), The development of subgrain
739 misorientations with strain in dry synthetic NaCl measured using EBSD. J. Struct. Geol.
740 27, 2159-2170.

741 Piazolo, S., P.D. Bons, M.W. Jessell, L. Evans, and C.W. Passchier (2002), Dominance of
742 microstructural processes and their effect on microstructural development: insights from
743 numerical modelling of dynamic recrystallization. Geol. Soc. Lon. Spec. Pub. 200, 149-
744 170.

745 Pennock, G. M., M. R. Drury, C. J. Peach, and C. J. Spiers (2006), The influence of water on
746 deformation microstructures and textures in synthetic NaCl measured using EBSD. J.
747 Struct. Geol. 28, 588-601.

748 Randle, V. (1993), Microtexture investigation of the relationship between strain and anomalous
749 grain growth. Philos. Mag. A 67.6, 1301-1313.

750 Randle, V., and O. Engler (2000), Introduction to Texture Analysis: Macrotexture, Microtexture
751 and Orientation Mapping. Gorden & Breach Science Publications.

752 Read, W. T., and W. Shockley (1950), Dislocation models of crystal grain boundaries. Phys.
753 Rev. 78.3, 275.

754 Schléder, Z., and J.L. Urai (2007), Deformation and recrystallization mechanisms in mylonitic
755 shear zones in naturally deformed extrusive Eocene-Oligocene rocksalt from Eyvanekey
756 plateau and Garmsar hills (central Iran). J. Struct. Geol. 29, 241-255.

757 Sethna, J. P., V. R. Coffman, and E. Demler (2003), Scaling in plasticity-induced cell-boundary
758 microstructure: Fragmentation and rotational diffusion. Physical Review B 67, 184107.

759 Signorelli, J., and A. Tommasi (2015), Modeling the effect of subgrain rotation recrystallization
760 on the evolution of olivine crystal preferred orientations in simple shear. Earth Planet.
761 Sci. Lett. 430, 356-366.

762 Steinbach, F., P. D. Bons, A. Griera, D. Jansen, M.-G. Llorens, J. Roessiger, and I. Weikusat
763 (2016), Strain localization and dynamic recrystallization in the ice-air aggregate: a
764 numerical study. The Cryosphere 10, 3071-3089.

765 Trimby, P. W., M.R. Drury, and C. J. Spiers (2000), Recognising the crystallographic signature
766 of recrystallization processes in deformed rocks: a study of experimentally deformed
767 rocksalt. J. Struct, Geol 22, 1609-1620.

768 Urai, J.L., W. D. Means, and G. S. Lister (1986), Dynamic recrystallization of minerals. In:
769 Hoobs, B. (Ed.), Mineral and Rock Deformation: Laboratory Studies: The Paterson
770 Volume, pp. 161-199.

771 Urai, J., Z. Schléder, C. Spiers, and P. A. Kukla (2008), Flow and Transport Properties of Salt
772 Rocks. In: Littke, R., Bayer, U., Gajewski, D., Nelskamp, S. (Eds.), Dynamics of
773 complex intracontinental basins: The Central European Basin System. Springer-Verlag,
774 Berlin Heidelberg, 277-290.

775 Wang, L., S. Blaha, T. Kawazoe, N. Miyajima, and T. Katsura (2017), Identical activation
776 volumes of dislocation mobility in the [100](010) and [001](010) slip systems in natural
777 olivine. Geophys. Res. Lett. 44, 2687-2692.

Weiss, L. E., and H. R. Wenk (1985), Preferred orientation in deformed metals and rocks: an introduction to modern texture analysis. Academic Press, London.

Wenk, H. -R., G. R. Canova, A. Molinari, and H. Mecking (1989), Texture development in halite: comparison of Taylor model and self-consistent theory. Acta Metall. 37, 2017-2029.

Wenk, H. -R., M. Armann, L. Burlini, K. Kunze, and M. Bortolotti (2009), Large strain shearing of halite: Experimental and theoretical evidence for dynamic texture changes. Earth and Planetary Science Letters 280, 205-210.

Figure captions

Figure 1. Initial model configuration, with the original orientation of grains. Three grains are selected for a more detailed analysis (shown in Figure 5). Orientations are shown with respect to the *x* axis.

Figure 2. Orientation and grain boundary map of a simulation SGC0 with only viscoplastic deformation, i.e., without recovery (SGC0). Orientations are shown with respect to the horizontal *x* axis. The trace of the shear plane is horizontal and the shear sense is dextral in this and the following figures.

Figure 3. Orientation and grain boundary map of a series of simulations with different degrees of recovery, at a shear strain of γ=1: (a-c) SGC0 (no recovery, only viscoplastic deformation), (d-f) SGC1, (g-i), SGC10, (j-l), SGC25 (1, 10 and 25 steps of recovery per deformation step, respectively). (a), (d), (g) and (j) show EBSD crystal orientation maps (as in Figure 2). (b), (e), (h) and (k) display misorientation maps. (c), (f), (i) and (l) show the misorientation with respect to the mean of the grain, using the original grains as reference (Figure 1). Note that in order to show details only one fourth of the model area is displayed.

Figure 4. Pole figures for the simulations shown in Figure 3. Stereograms on the left and right groups of columns show the CPO evolution for the simulations without recovery (SGC0) and with 25 steps of recover per deformation time step (SGC25), respectively. Equal area projection, with linear contour intervals. The pole figures show that the addition of the recovery process has remarkably little effect on the CPO's.

Figure 5. Orientation and grain boundary maps showing details of three selected grains (see Figure 1 for their original orientation and geometry) in the models with SGC0 and SGC10 at γ=1.The addition of subgrain coalescence reduces subgrain boundary misorientations and reduces the crystal orientation spread and the formation of grain and subgrain boundaries. Note that the color coding for grain boundaries is the same as in Figures 2 and 3.

Figure 6. Evolution with progressive strain of the slip system activity for the different simulations, calculated as the average of all *unodes* or crystallites in the simulation.

Figure 7. Distribution of the slip system activity for the SGC0 simulation, at two deformation stages: (a) γ=0.04 and (b) γ=1.

Figure 8. Frequency distribution of grain geometric mean misorientations for different deformation stages (expressed in terms of shear strain γ), for all the experiments performed. Geometric means of misorientation distributions $\theta_{mean\text{-}grains}$ are indicated, together with the standard deviation of the mean. Misorientations were calculated with respect to the grains at the current time step, considering that grains form when the misorientation is higher than 15º. The total number of grains is also displayed as an indication of the intensity of grain size reduction. The value in parentheses corresponds to the number of grains that contain at least ten crystallites, and which are considered for the strain gauge discussed in section 4 (see below).

Figure 9. Weighted geometric mean of grain misorientation as a function of natural strain, calculated with equation (8). Geometric means are weighted according to the number of

825 crystallites per grain. Only grains with a minimum of ten crystallites are considered for the
826 calculation. Solid lines show the theoretical power-law relationship for experiments with
827 different intensity of intracrystalline recovery using the k_1 values listed in the legend and a
828 universal n exponent of 2/3 (see discussion section). The R^2 coefficients are calculated with
829 respect to this scaling law. Dashed lines show the best fit for each model (with R^2), with
830 exponents of 0.81 (SGC0), 0.76 (SGC1), 0.66 (SGC10) and 0.53 (SG25). The experimental data
831 from *Pennock et al.* [2005] are displayed and used to calculate the power-law relationship for the
832 experiment without recovery (SGC0) (thick solid line). These data are used as a reference to
833 normalize the results of our series of numerical simulations, at ε=1.

834

Figure 1.

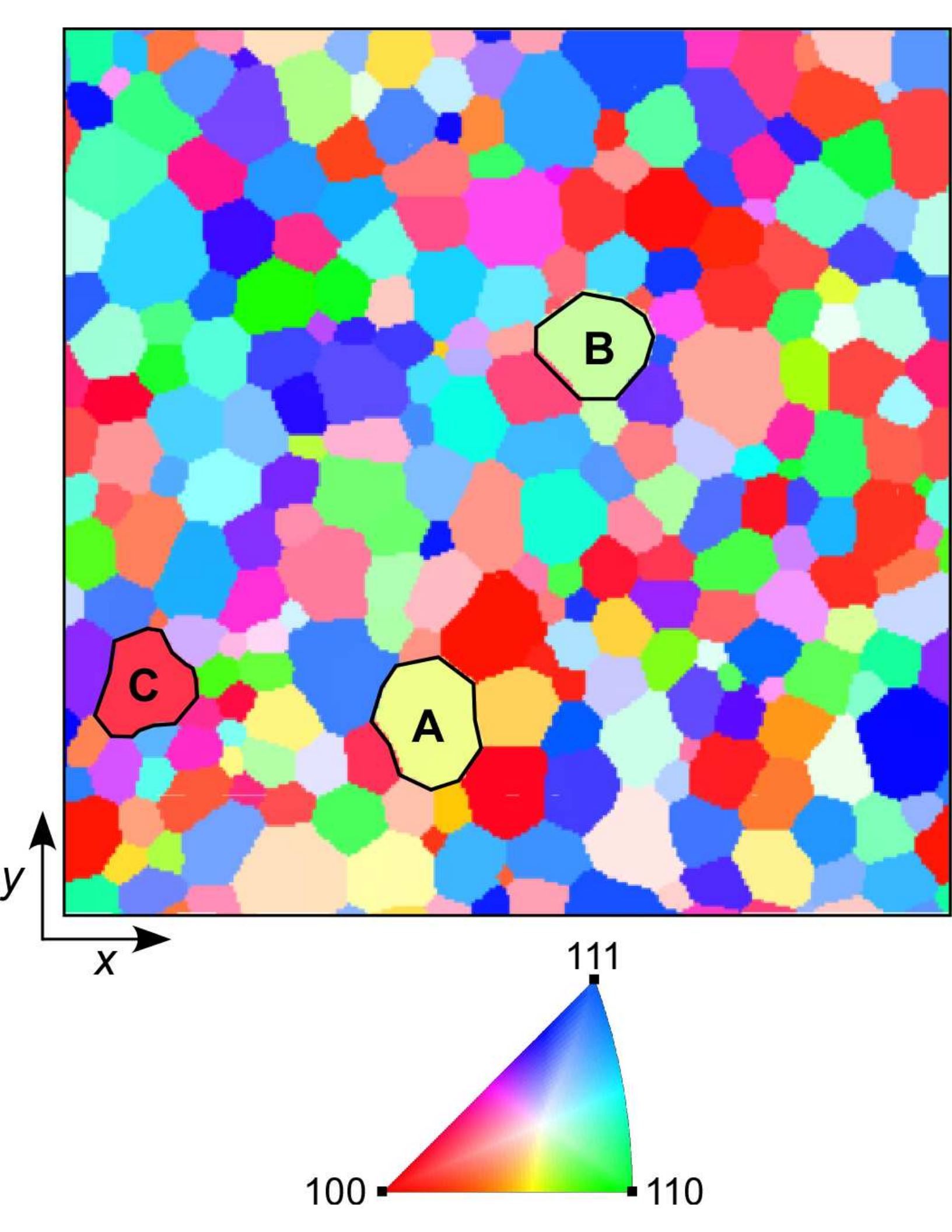
B
C
A
y
x
111
100
110

Figure 2 (revised).

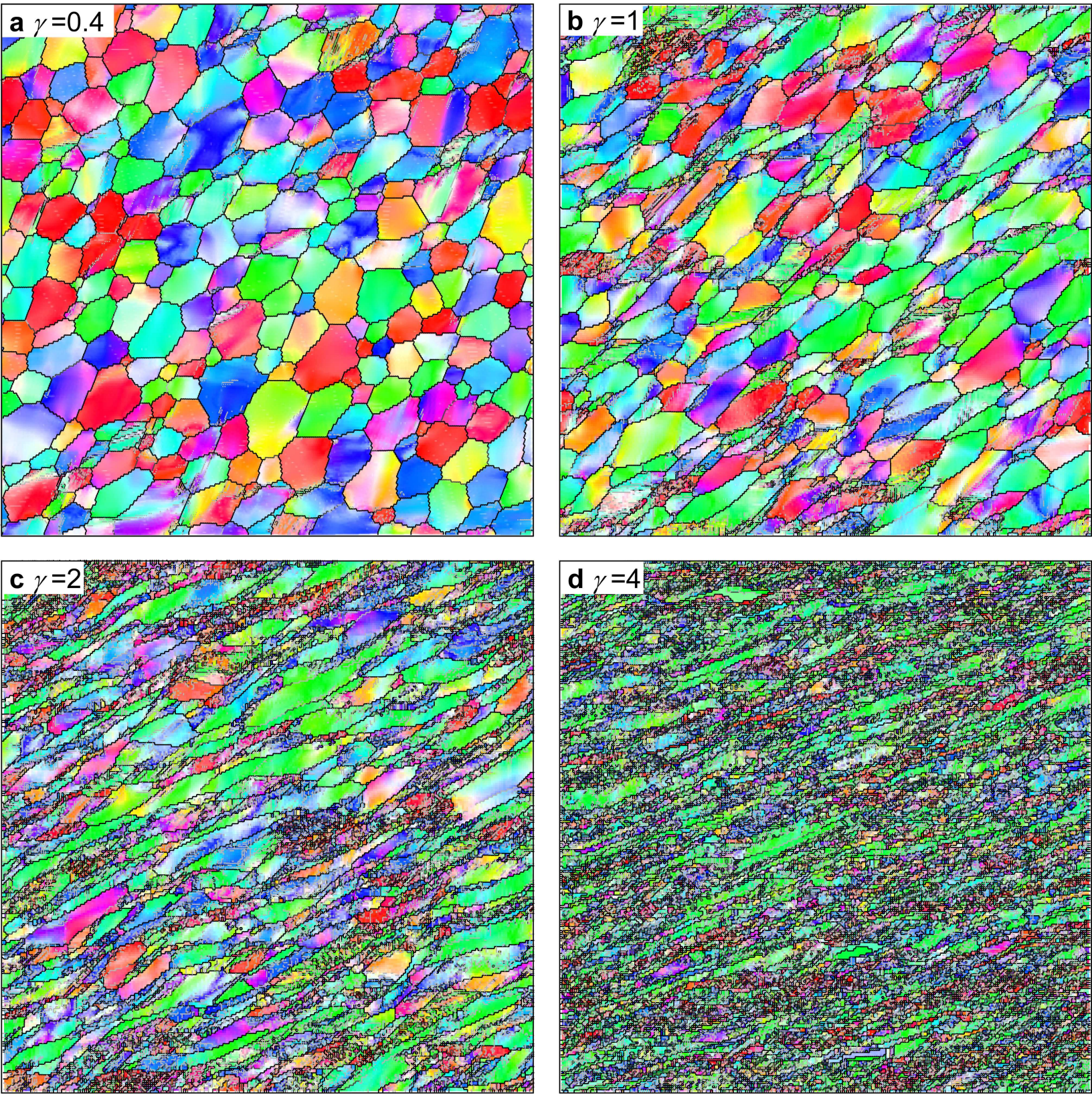
a γ=0.4
b γ=1
c γ=2
d γ=4
grain and subgrain boundaries:
5º - 10º
10º - 15º
>15º
111
100
110

Figure 3.

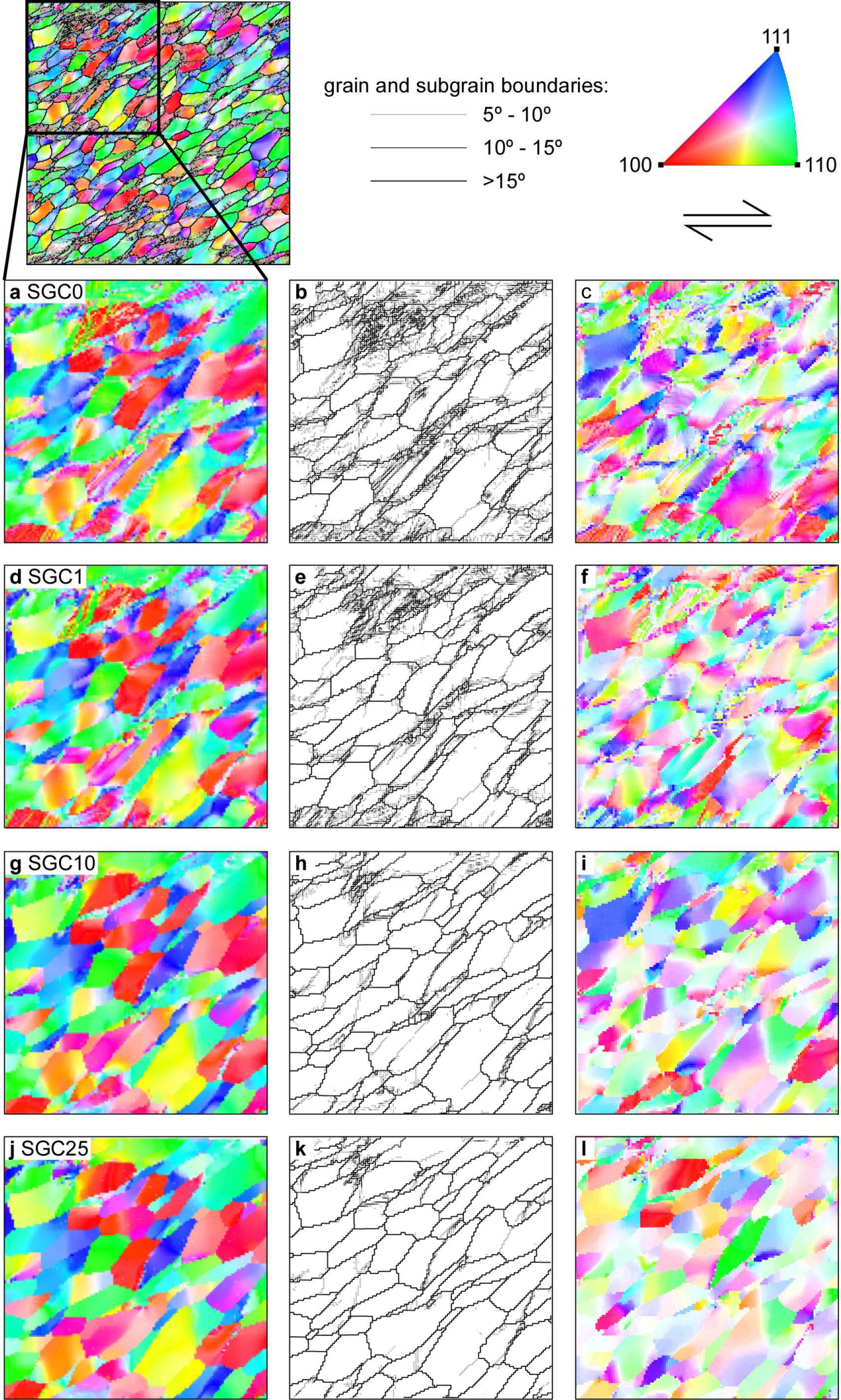
grain and subgrain boundaries:
5° - 10°
10° - 15°
>15°
111
100
110
a SGC0
b
c
d SGC1
e
f
g SGC10
h
i
j SGC25
k
l

Figure 4.

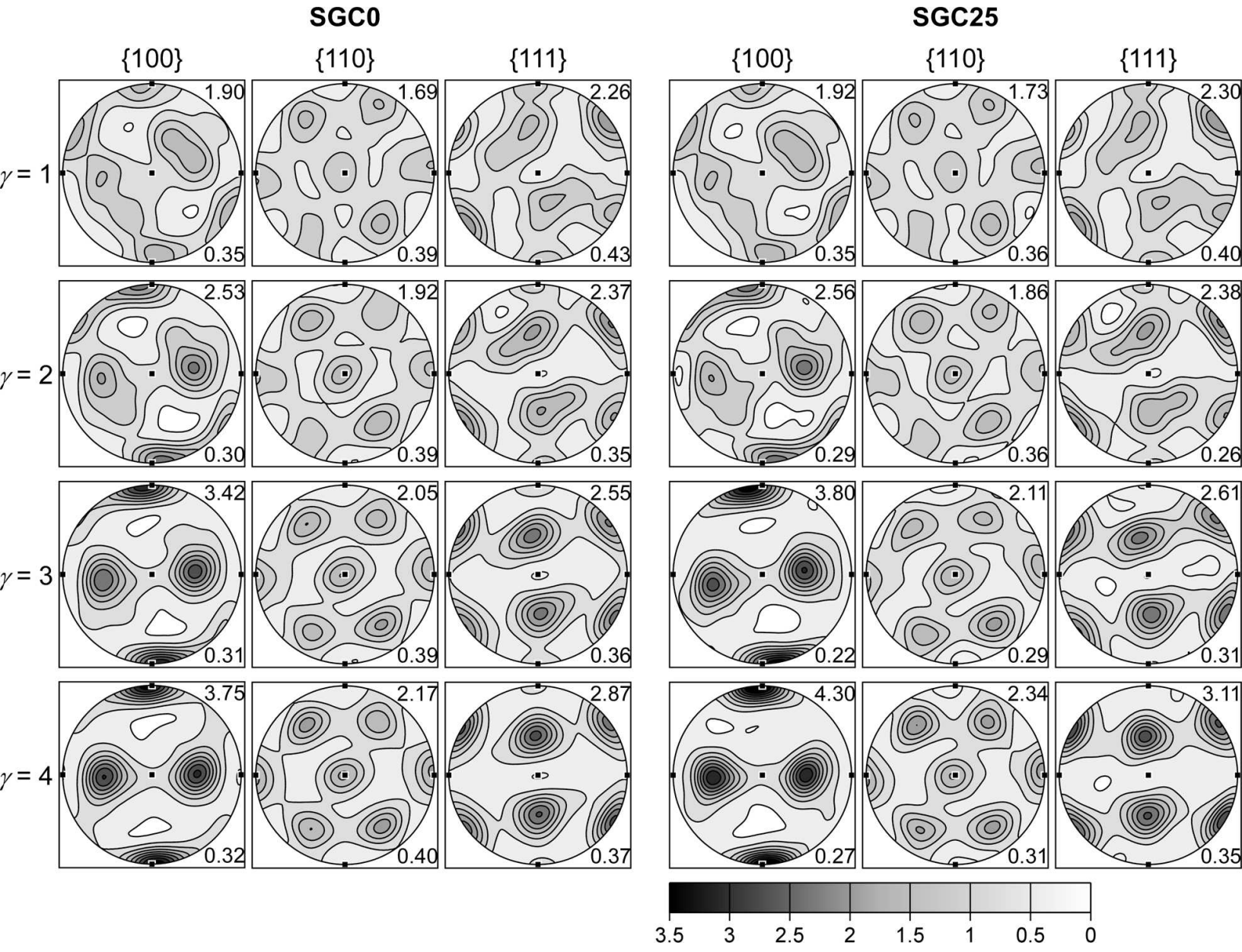
SGC0
SGC25
{100}
{110}
{111}
{100}
{110}
{111}
γ = 1
γ = 2
γ = 3
γ = 4
1.90
0.35
1.69
0.39
2.26
0.43
1.92
0.35
1.73
0.36
2.30
0.40
2.53
0.30
1.92
0.39
2.37
0.35
2.56
0.29
1.86
0.36
2.38
0.26
3.42
0.31
2.05
0.39
2.55
0.36
3.80
0.22
2.11
0.29
2.61
0.31
3.75
0.32
2.17
0.40
2.87
0.37
4.30
0.27
2.34
0.31
3.11
0.35
3.5
3
2.5
2
1.5
1
0.5
0

Figure 5.

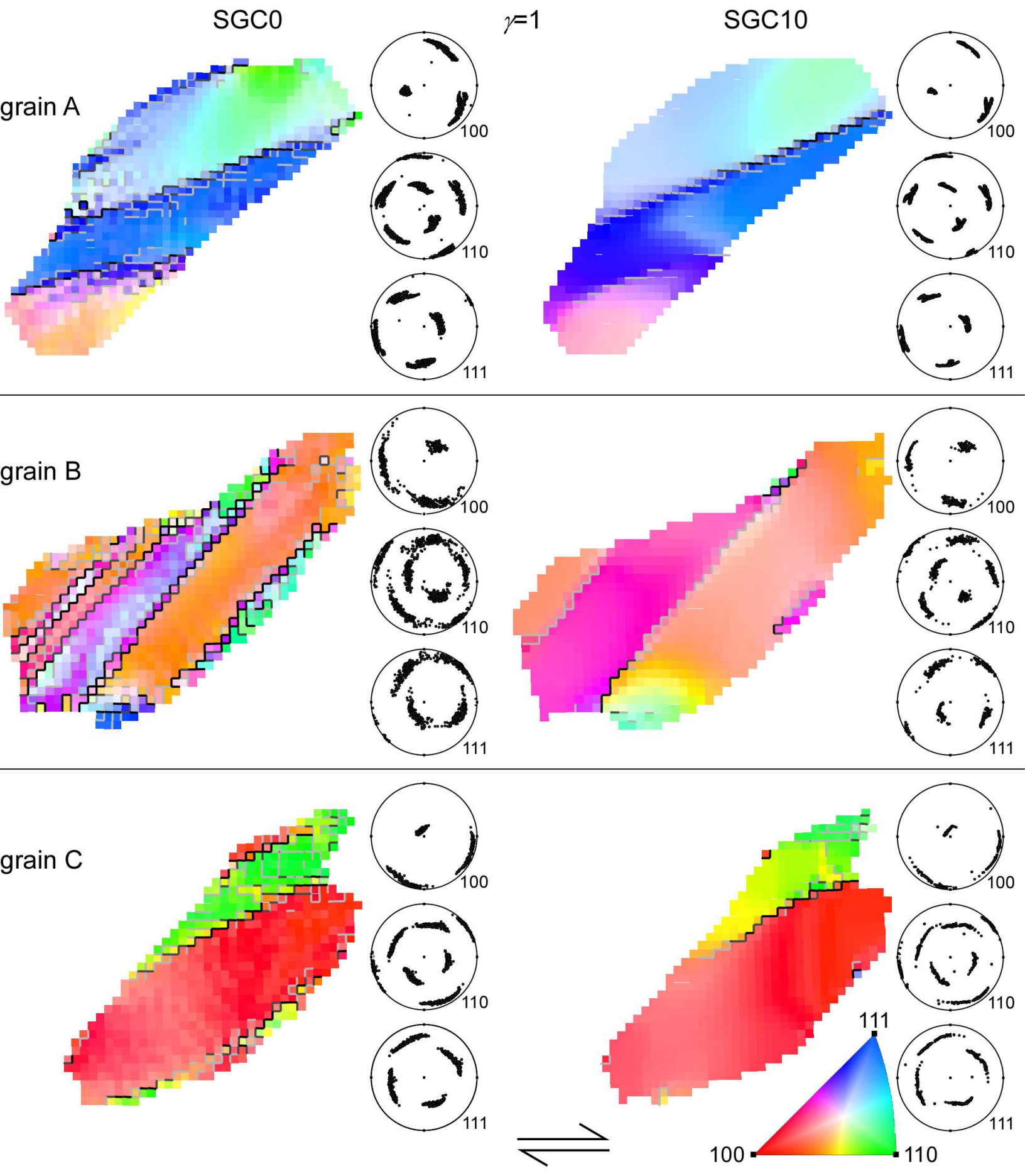
SGC0
γ=1
SGC10
grain A
grain B
grain C
100
110
111
100
110
111
111
100
110

Figure 6 (revised).

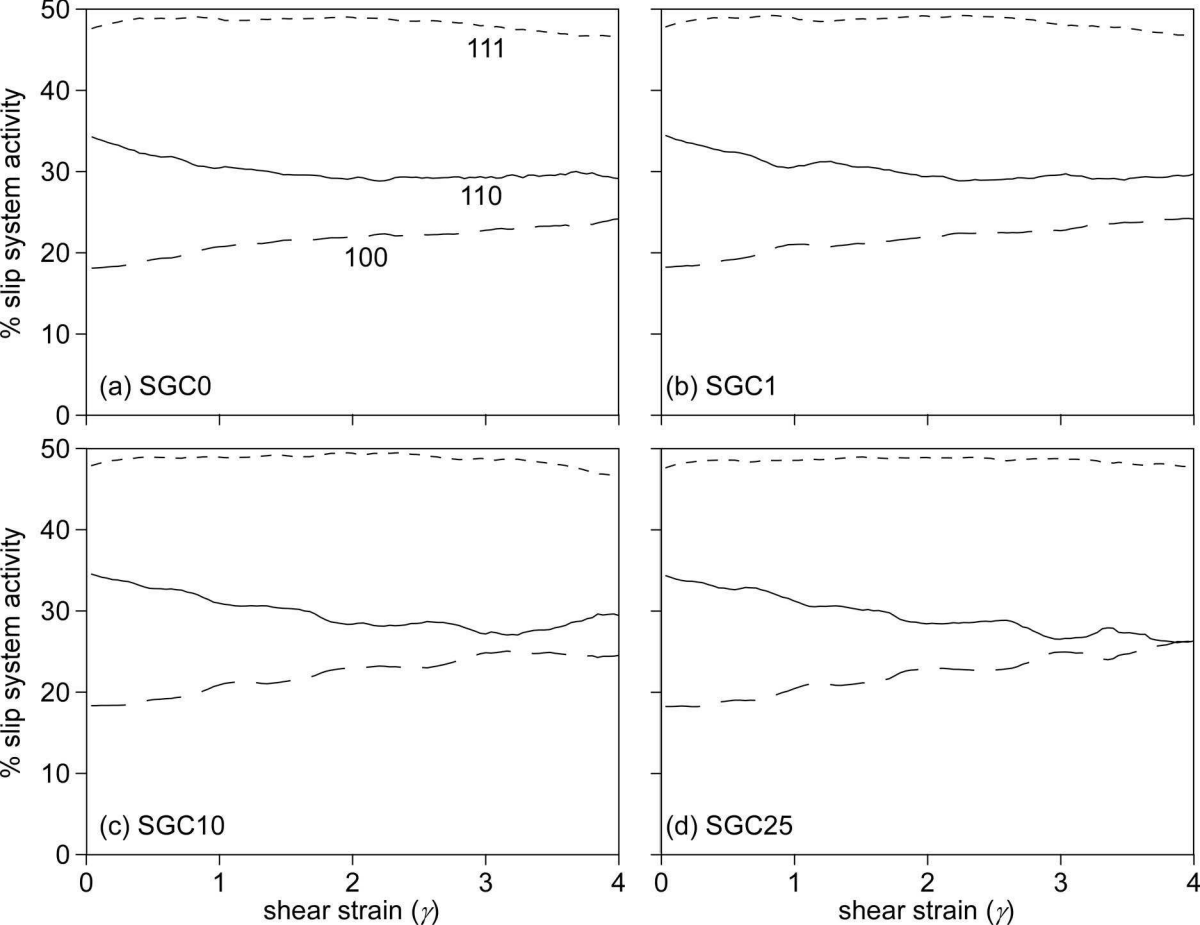
% slip system activity
50
40
30
20
10
0
111
110
100
(a) SGC0
(b) SGC1
(c) SGC10
(d) SGC25
0
1
2
3
4
shear strain (γ)

Figure 7.

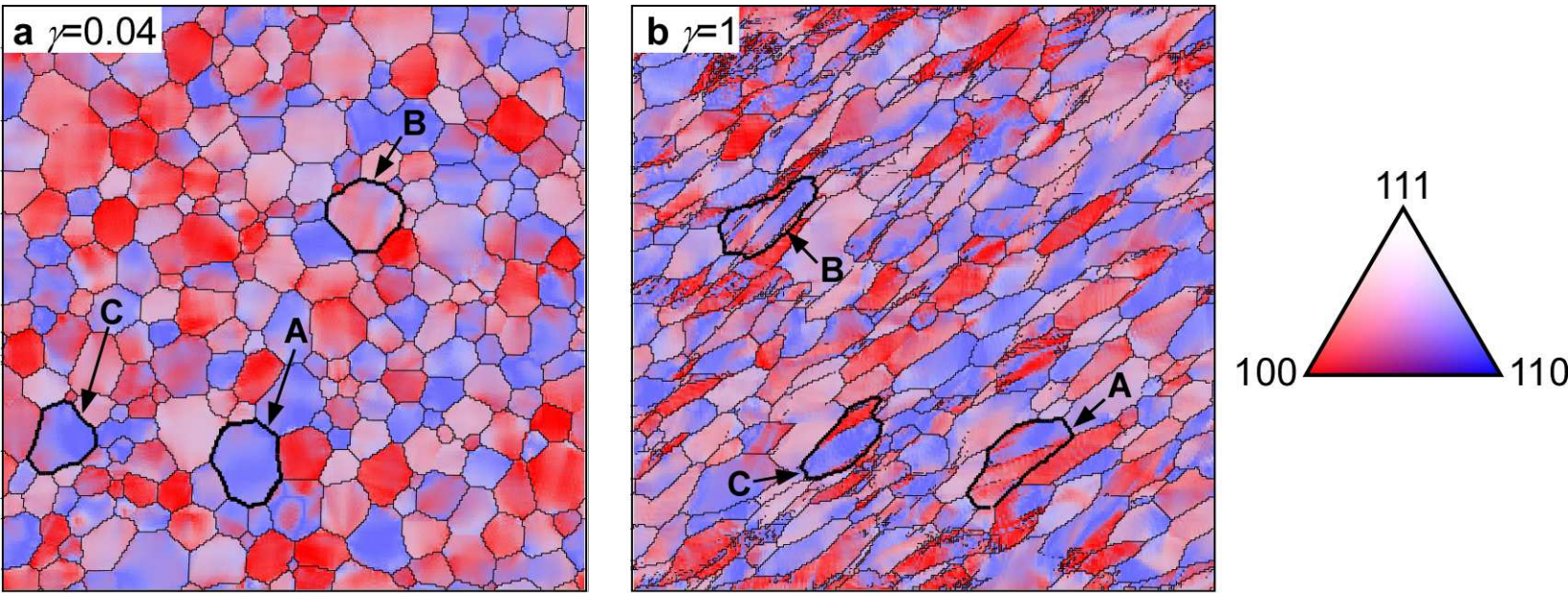
a γ=0.04
B
C
A
b γ=1
B
A
C
111
100
110

Figure 8 (revised).

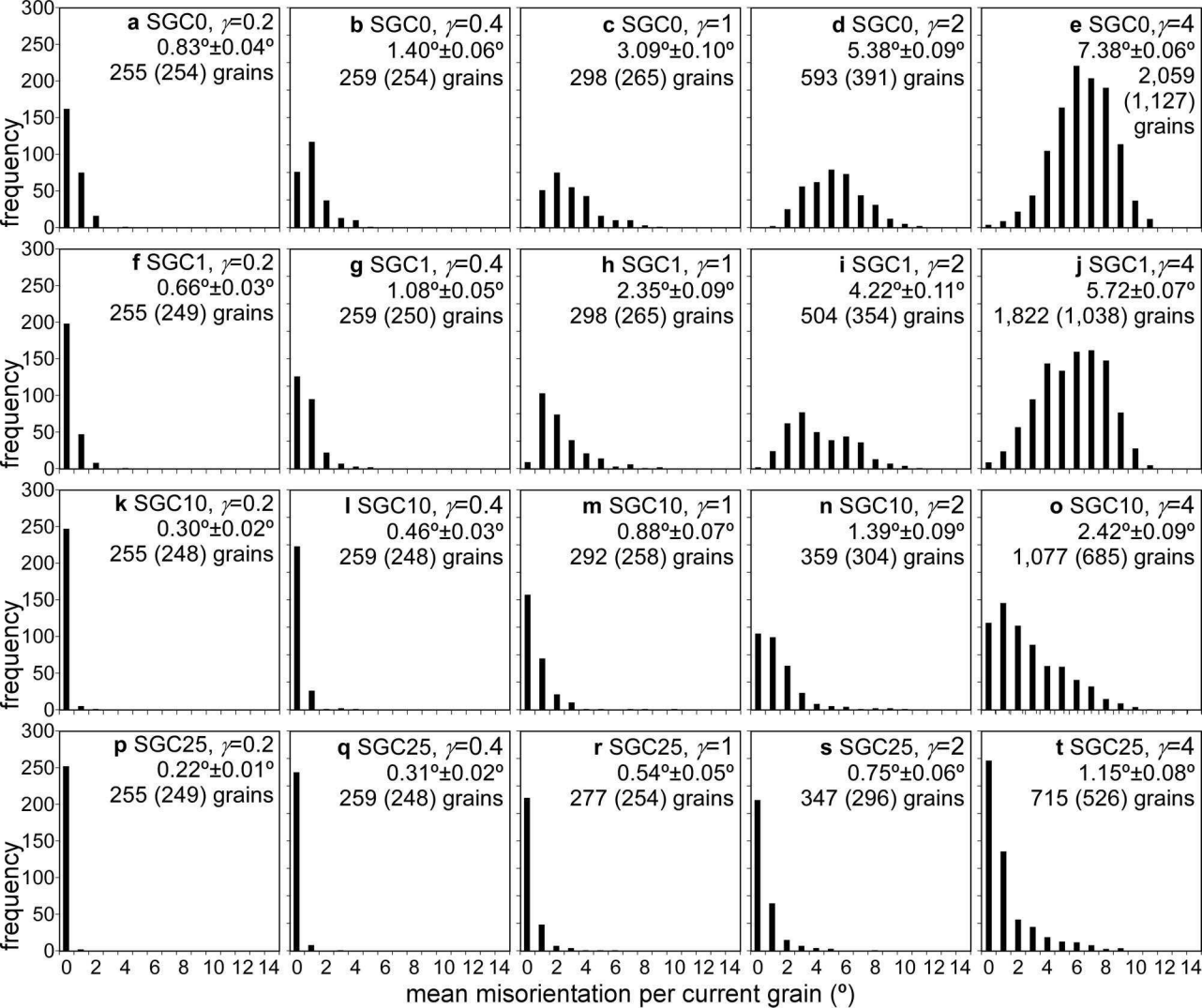
a SGC0, γ=0.2
0.83°±0.04°
255 (254) grains
b SGC0, γ=0.4
1.40°±0.06°
259 (254) grains
c SGC0, γ=1
3.09°±0.10°
298 (265) grains
d SGC0, γ=2
5.38°±0.09°
593 (391) grains
e SGC0, γ=4
7.38°±0.06°
2,059
(1,127)
grains
f SGC1, γ=0.2
0.66°±0.03°
255 (249) grains
g SGC1, γ=0.4
1.08°±0.05°
259 (250) grains
h SGC1, γ=1
2.35°±0.09°
298 (265) grains
i SGC1, γ=2
4.22°±0.11°
504 (354) grains
j SGC1, γ=4
5.72±0.07°
1,822 (1,038) grains
k SGC10, γ=0.2
0.30°±0.02°
255 (248) grains
l SGC10, γ=0.4
0.46°±0.03°
259 (248) grains
m SGC10, γ=1
0.88°±0.07°
292 (258) grains
n SGC10, γ=2
1.39°±0.09°
359 (304) grains
o SGC10, γ=4
2.42°±0.09°
1,077 (685) grains
p SGC25, γ=0.2
0.22°±0.01°
255 (249) grains
q SGC25, γ=0.4
0.31°±0.02°
259 (248) grains
r SGC25, γ=1
0.54°±0.05°
277 (254) grains
s SGC25, γ=2
0.75°±0.06°
347 (296) grains
t SGC25, γ=4
1.15°±0.08°
715 (526) grains
frequency
0 50 100 150 200 250 300
0 2 4 6 8 10 12 14
mean misorientation per current grain (°)

Figure 9 (revised).

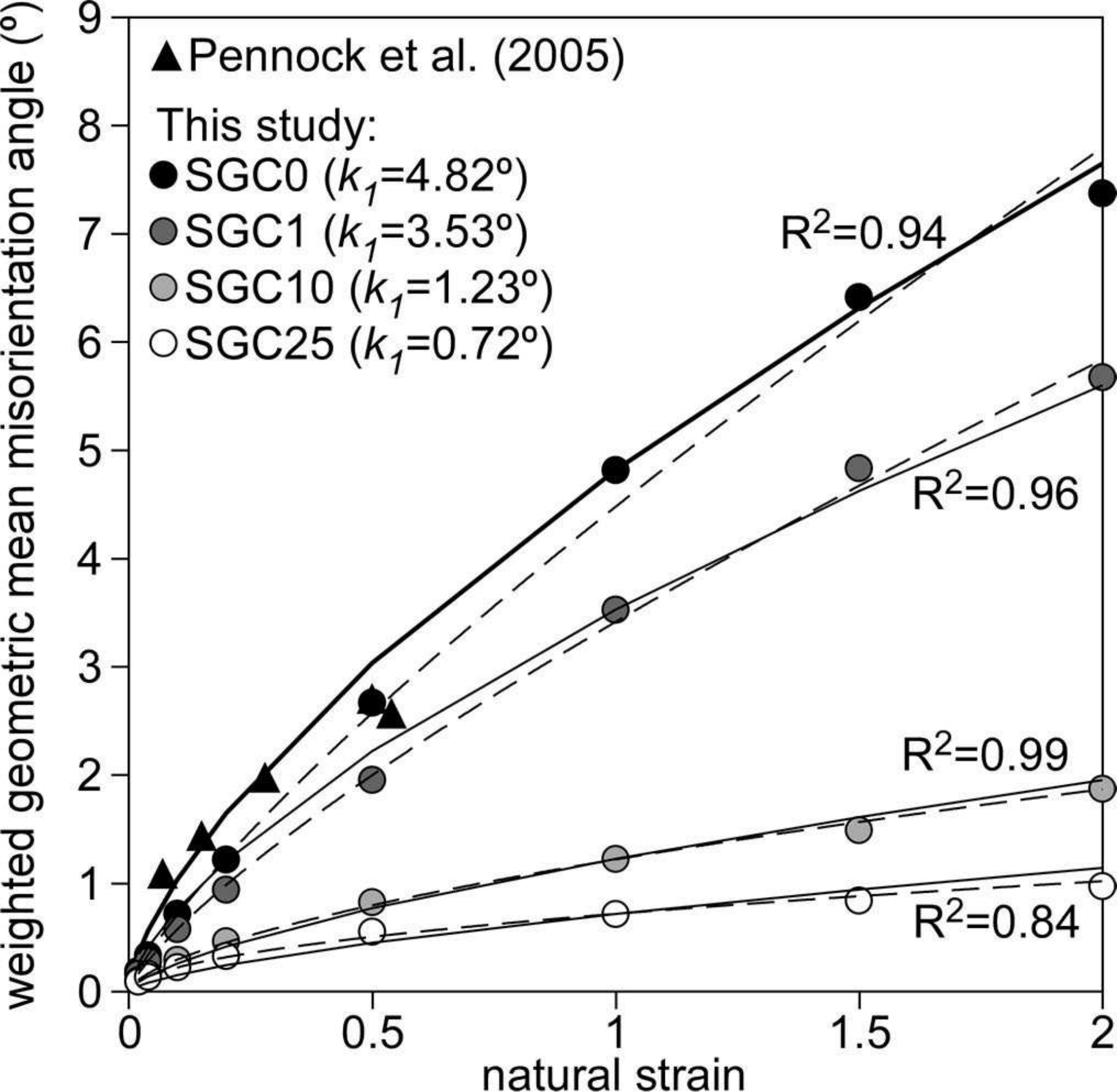
Pennock et al. (2005)
This study:
SGC0 (k_1=4.82º)
SGC1 (k_1=3.53º)
SGC10 (k_1=1.23º)
SGC25 (k_1=0.72º)
R^2=0.94
R^2=0.96
R^2=0.99
R^2=0.84
weighted geometric mean misorientation angle (º)
natural strain
0
1
2
3
4
5
6
7
8
9
0
0.5
1
1.5
2